

Elastic secondary flows of semidilute DNA solutions in abrupt 90° microbends

Shelly Gulati,¹ Dorian Liepmann,^{1,2} and Susan J. Muller^{1,3}

¹UCSF/UCB Joint Graduate Group in Bioengineering, University of California, Berkeley, California 94720, USA

²Department of Bioengineering, University of California, Berkeley, California 94720, USA

³Department of Chemical Engineering, University of California, Berkeley, California 94720, USA

(Received 1 June 2008; published 16 September 2008)

Secondary flows that are absent in Newtonian flows are found for semidilute λ -DNA solutions in abrupt planar 90° microbends at modest levels of elasticity. Flow visualization and microparticle image velocimetry experiments show that a vortex, which is present in the inner, upstream corner of the bend, grows with increasing Reynolds and Weissenberg number ($9.9 \times 10^{-7} < \text{Re} < 3.1 \times 10^{-2}$, $0.41 < \text{Wi} < 126$). The vortex growth is quantified as a function of elasticity; at high elasticity, the vortex occupies a significant fraction of the upstream channel and distorts the primary flow. The presence of elastic vortices, in which molecules can become trapped for long times, has implications for the design of microdevices for the processing of biological macromolecules.

DOI: 10.1103/PhysRevE.78.036314

PACS number(s): 47.50.-d, 83.80.Rs, 47.61.Fg

INTRODUCTION

Understanding the complex behavior of macromolecular flow in microfluidic geometries is critical to the realization of lab-on-a-chip and micro total analysis systems (μ TAS) intended to systematically manipulate, process, and analyze these molecules. In sufficient concentrations, the presence of macromolecules, such as DNA, gives the fluid viscoelastic behavior that may alter the base flow or lead to flow instabilities for flows along curved streamlines [1–4]. This is particularly important in microfluidic devices in which canonical elements force fluids to traverse regions of abruptly varying cross-sectional area or curved paths, commonly with sharp corners.

Elasticity has long been known to give rise to secondary flows; as noted by Bird *et al.* [1], these elastic secondary flows are often in the opposite direction of those caused by inertial effects. For example, *Newtonian* flow in a fluid-filled cylinder driven by the motion of a rotating lid exhibits a primary tangential flow and a centrifugally driven secondary flow directed radially outward near the disk, down the sides of the cylinder, and back upward along the cylinder axis. Elasticity drives the secondary flow in this system in the opposite direction: radially inward near the disk, down along the cylinder axis, and up the sides of the cylinder.

Elasticity, even in the limit of vanishing inertia (Reynolds numbers much less than unity), may also make the base flow unstable to disturbances; such elastic instabilities occur above a critical condition, typically as a result of the coupling of curvature of fluid streamlines and elastic normal stresses that impart a tension along the streamlines. Purely elastic instabilities have been well documented experimentally and numerically for viscoelastic fluids in (macroscale) Taylor-Couette flow, Taylor-Dean flow, torsional flow between parallel disks, and complex geometries such as abrupt contractions [2–6]. The kinematic curvature of the streamlines and the dynamic influence of the viscoelastic normal stresses can be combined, via scaling arguments, into a universal criterion to describe the condition that must be exceeded for the onset and growth of elastic instabilities for

two-dimensional (2D) creeping flows in curved geometries [3,4]. The general form for the criterion M_{crit} is represented by the following:

$$\left(\frac{\lambda U}{R} \frac{\tau_{11}}{(\eta_0 \dot{\gamma})} \right)^{1/2} \geq M_{\text{crit}}, \quad (1)$$

where λ is the relaxation time of the fluid, U is the characteristic streamwise fluid velocity, R is the characteristic radius of curvature of the streamline, τ_{11} is the normal stress in the flow direction, η_0 is the zero-shear-rate viscosity of the fluid, and $\dot{\gamma}$ is the characteristic value of the local deformation rate in the flow. Elastic instabilities in Taylor-Couette flows, torsional flow between a cone and plate, lid-driven cavity flows, and flows past a cylinder are all well described by M_{crit} values in the range of 4.6 to 8.4 [4]. However, the numerical value of M_{crit} varies with flow geometry and cannot be determined without a detailed numerical or experimental analysis of a particular geometry. In addition, we note that the criterion does not differentiate between elastic instabilities in purely shearing flows and those with both shearing and extensional components, nor does it explicitly describe the important role that normal stresses in the gradient direction (i.e., τ_{22}) may play in the stability of viscoelastic flows. Nonetheless, Eq. (1) provides a simple, useful means of estimating when elastic instabilities may occur in a wide range of geometries.

Viscoelastic flows have been explored in a number of microfluidic geometries for a variety of applications. Viscoelastic flows and the growth of elastic instabilities have been studied in microfluidic planar abrupt contractions, a viscoelastic benchmark geometry [7–9]. Elastic secondary flows and instabilities have been explored for microfluidic mixing applications in serpentine channels [10–12] and cross-slot microchannels [13]. Elastic instabilities have also been harnessed for operation of a microfluidic flow rectifier [14].

Newtonian flows in curved channels of rectangular cross section have also been studied in detail both at the macroscale and at the microscale; here the important parameter is the Dean number κ , defined as $\kappa = (\rho U D_h / \eta) (D_h / 2R)^{0.5}$

where ρ is the solution density, U is the average channel velocity, D_h is the hydraulic diameter, η is the solution viscosity, and R is the radius of curvature of the channel. At low Dean numbers, a secondary flow consisting of two counter-rotating vortices (perpendicular to the primary flow, with one above and one below the symmetry plane) results from centrifugal forces; above a critical Dean number ($\kappa \sim 100$), the flow becomes unstable through a bifurcation to a flow characterized by the appearance of an additional pair of counter-rotating vortices in the cross-sectional plane. Recently, use of both secondary flows and instabilities in Newtonian flows in curved microchannels has been explored numerically [15] and experimentally [16–18] for their potential as micromixing elements.

In this paper, we document an elastic secondary flow for viscoelastic flows in sharp 90° microbends or L-shaped channels. The channels are rectangular in cross section and have the same dimensions upstream and downstream of the sharp corner. The flow is parametrized by a Reynolds number $Re = \rho U D_h / \eta$ and a Weissenberg number $Wi = \lambda \dot{\gamma}$, where λ is the relaxation time of the polymer and $\dot{\gamma}$ is a characteristic shear rate. Very little previous work on this flow exists. Numerical simulations for the steady 2D flow in an L-shaped channel indicate that, at low Re , elasticity leads to modest deviations from the Newtonian case, with a slight shift in the streamlines toward the outer wall [19,20]. Two sets of experiments exist in macroscale L-shaped channels. Cochrane *et al.* [21] examined a non-shear-thinning, viscoelastic (i.e., Boger) fluid in a channel that was 1.2 cm wide and only 2.0 cm deep (in the direction perpendicular to the flow) for Re of 4 and 16 and Wi numbers of 0, 0.3, and 0.14. These authors reported negligible changes due to elasticity relative to the Newtonian case. Chono and Iemoto [22], in a channel that was 50 mm wide and 250 mm deep, studied a shear-thinning viscoelastic fluid for conditions near $Re \sim 1$, $Wi \sim 1$, and reported a slight shift in streamlines consistent with their 2D numerical simulations. These authors also considered varying ratios of upstream and downstream channel widths, and observed a small, viscoelastic recirculation region at the inside, upstream corner when the upstream channel was significantly wider than the downstream channel. To our knowledge, the appearance and growth of the elastic vortex upstream of the corner have not been previously observed in the present geometry with up- and downstream channels of equal widths, in either microscale or macroscale flows. The vortex is absent in Newtonian fluids, and thus is not associated with centrifugal forces that result in Dean vortices in continuously curved channels.

EXPERIMENT

We study a semidilute DNA solution flowing in an abrupt, planar 90° microbend fabricated in silicon. The microbend or L-shaped channel device consists of two straight channels of rectangular cross section that are both $200 \mu\text{m}$ wide and $225 \mu\text{m}$ deep and meet at a 90° angle to create a sharp elbow or L shape. Each channel is connected to a reservoir, and has a total length of 6 mm between the reservoir and the junction, ensuring that the flow is fully developed well upstream

TABLE I. Experimental operating space.

	Water	400 $\mu\text{g}/\text{ml}$ DNA
Re	0.033–0.26	9.9×10^{-7} – 3.1×10^{-2}
Wi	0	0.41–126
El	0	4.2×10^5 – 4.1×10^3
κ	0.041–0.33	1.3×10^{-6} – 3.9×10^{-2}
c/c^*	0	4

and well downstream of the bend. Vertical channel walls are produced through the use of deep reactive ion etching and the device is sealed by anodically bonding a Pyrex glass wafer to the silicon device; details of the fabrication process have been reported elsewhere [9,23].

Flows of water and semidilute DNA solutions (λ -bacteriophage DNA, 31.5×10^6 Da, 48 502 base pairs) are explored in this geometry. The DNA solution is diluted to a concentration of 400 $\mu\text{g}/\text{ml}$ using a buffer (1×40 mM Tris acetate and 1 mM ethylene diamine tetraacetic acid (EDTA), pH 8.3); this concentration is four times the overlap concentration (c^*) for the DNA solution. Rheological properties were characterized using oscillatory flow capillary viscometry and steady and dynamic shear rheometry. The $4c^*$ DNA solution is found to be highly shear thinning at high shear rates, with a shear viscosity η described by the power law $\eta = 0.136 \dot{\gamma}^{-0.813}$ (where $\dot{\gamma}$ is expressed in s^{-1} and η has units of Pa s). The relaxation time is determined from a fit of the experimental dynamic rigidity and dynamic viscosity to a multimode generalized Maxwell model. The detailed rheological characterization of the DNA solution is included in Refs. [9,23].

We report the Reynolds number based on the shear-rate-dependent viscosity, i.e., $Re = \rho U D_h / \eta(\dot{\gamma})$. The longest relaxation time λ is found from the Maxwell fit to be 6.79 s for the DNA solution; this is the relaxation time used in our calculations of Wi . The characteristic shear rate $\dot{\gamma}$ in Wi is taken to be the average velocity U divided by the channel half width $w/2$. We also report an elasticity number El , defined as the ratio of Weissenberg and Reynolds numbers, i.e., $El = Wi/Re$. For completeness, we compute an effective Dean number κ in which R is taken as the radius of curvature of a streamline at the midline of the microbend. Parameter ranges examined in this study are summarized in Table I. For the $4c^*$ DNA solution, Reynolds numbers and Dean numbers are always much less than unity, Weissenberg numbers vary from 0.4 to 126, and elasticity numbers vary from 4.1×10^3 to 4.2×10^5 .

The test fluids are seeded with fluorescent polystyrene tracer particles ($1 \mu\text{m}$ diameter FluoSpheres, Molecular Probes) for flow visualization and are driven through the microbend using a syringe pump. Images were obtained using an epifluorescence microscope with a mercury burner and neodymium-doped yttrium aluminum garnet (Nd:YAG) lasers as illumination sources for streak images and micro-particle image velocimetry (μPIV), respectively. Streak images and video microscopy reveal the flow kinematics in the microbend and μPIV is used to quantify the velocity field in the vicinity of the bend. Implementation of the streak imag-

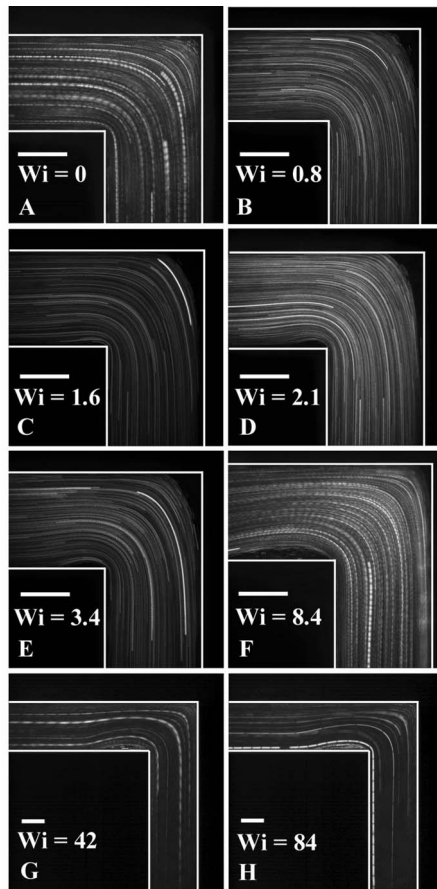


FIG. 1. Streak images of the abrupt microbend for flow of water at (a) $Re=0.033$ and for flow of the $4c^*$ DNA solution at (b) $Re=3.4 \times 10^{-6}$, $Wi=0.8$, (c) $Re=1.1 \times 10^{-5}$, $Wi=1.6$, (d) $Re=1.8 \times 10^{-5}$, $Wi=2.1$, (e) $Re=4.3 \times 10^{-5}$, $Wi=3.4$, (f) $Re=2.3 \times 10^{-4}$, $Wi=8.4$, (g) $Re=4.2 \times 10^{-3}$, $Wi=42$, and (h) $Re=1.5 \times 10^{-2}$, $Wi=84$. The scale bars are $100 \mu\text{m}$. Fluid enters the channel at the left in each figure, and exits at the bottom.

ing and microparticle image velocimetry is as described in [9,23].

RESULTS

Streak images of the flow in the microbend are given in Fig. 1 and were constructed by overlaying sequential fluorescence images for an exposure time of 4 s. In each of the images, the fluid enters the channel upstream of the left edge of the image, flowing from left to right across the image and then downward through the perpendicular channel (exiting the frame at the bottom of each image). Figure 1(a) reveals that for flows of distilled water no vortices are evident. Across the parameter range probed for the Newtonian flows ($0.033 < Re < 0.26$), no secondary flows or flow instabilities were found. This corresponds to the Dean number range $0.033 < \kappa < 0.26$ and the behavior is consistent with the observation that the existence of a strong secondary flow generally occurs for $\kappa > 10$ [24].

For flows of $4c^*$ DNA at low Wi [Fig. 1(b)] no vortex was present, consistent with behavior for the Newtonian fluid.

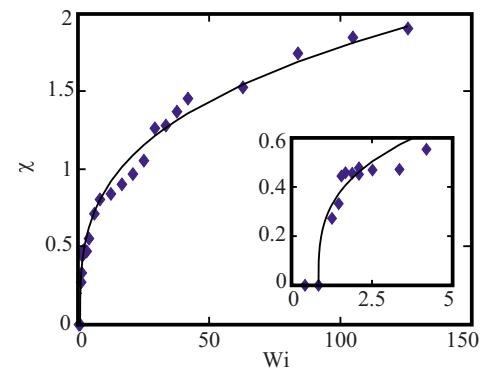


FIG. 2. (Color online) Average dimensionless vortex length for flows of the $4c^*$ DNA solution through the 90° microbend device as a function of Wi . The vortex length follows the functional form, $\chi=0.43(Wi-Wi_{crit})^{0.31}$ where Wi_{crit} is 0.84.

With a modest increase in Wi , however, a vortex develops in the inner, upstream corner of the 90° microbend [Fig. 1(c)]. This elastic secondary flow is evident for $Wi > 0.84$. The corner vortex grows dramatically with increasing Re and Wi [Figs. 1(d)–1(h); note the change in magnification between images Figs. 1(f) and 1(g)], revealing the strong effect of elasticity on the flow. Over the parameter range probed, the corner vortices are stable and not time dependent.

The vortex length L_V was obtained by measuring the distance along the inner, upstream wall from the edge of the vortex boundary to the corner of the microbend. The dimensionless vortex length χ was then computed by normalizing L_V by the channel width w ($200 \mu\text{m}$). Figure 2 shows the relationship between the dimensionless vortex length χ and Wi for flows of $4c^*$ DNA. The growth of the dimensionless vortex length is fairly well described by the functional form $\chi=0.43(Wi-Wi_{crit})^{0.31}$ where Wi_{crit} is 0.84. The inset indicates the transition from Newtonian-like flow ($\chi=0$) for $Wi < Wi_{crit}$ to the onset of the secondary flow ($\chi > 0$) for $Wi > Wi_{crit}$.

Velocity fields constructed using μPIV can be used to quantify the magnitude of the flow around the bend as well as the strength of the secondary flow. The velocity vector field for the primary flow of $4c^*$ DNA at $Wi=42$, $Re=4.2 \times 10^{-3}$ is given in Fig. 3(a). The bend position located at $x/w=0$ and the centerline of the channel upstream of the bend is located at $y/w=0$, where we are normalizing the x and y positions by the channel width w . Velocities are normalized by the average velocity U . Interrogation regions for μPIV were $\sim 28 \times 28 \mu\text{m}^2$ with a 50% overlap for the primary flow velocity field.

The presence of the vortex acts to constrict the flow in the channel upstream of the bend creating a smaller effective channel diameter in this region. As a result, not only is the primary flow perturbed far upstream (beyond the field of view) due to the presence of the bend, but it also feels the effect of the constriction created by the vortex. Additionally, the fluid must accelerate to pass the vortex region yielding a larger effective shear rate in the primary flow than would be predicted from the channel dimensions.

Since the flow within the vortex is significantly slower than the primary flow, the velocity vector field given in Fig.

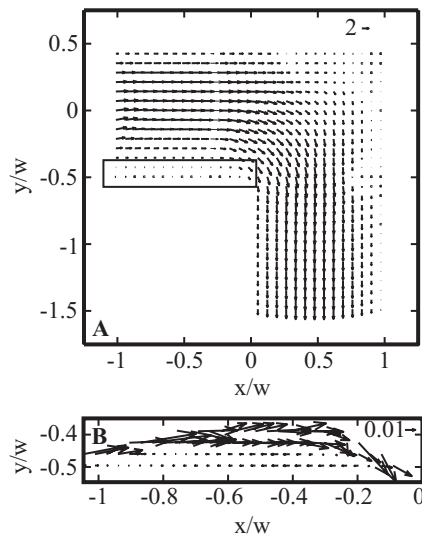


FIG. 3. Flow of the $4c^*$ DNA solution through the 90° microbend at $Re=4.2 \times 10^{-3}$, $Wi=42$. (a) Velocity vector field for primary flow. (b) Velocity vector field in the vortex. This field was constructed with smaller interrogation regions and imaging at the same magnification. The x and y positions are normalized by the channel width ($w=200 \mu\text{m}$). The bend is located at $x/w=0$ and the centerline is located at $y/w=0$. Velocities are normalized by the average velocity. The reference arrows are $v/U=2$ and 0.01 for the primary and secondary flows, respectively.

3(b) can be obtained at a higher spatial resolution. Here the interrogation regions were $\sim 14 \times 14 \mu\text{m}^2$ with a 50% overlap for the velocity field of the secondary flow. At this higher spatial resolution the vortex velocity field reflects the observations from video microscopy of small negative velocities near the walls and large positive velocities near the vortex boundary.

Because the vortex growth is not accompanied by a change in the time dependence or dimensionality of the flow (i.e., the flow remains steady and three dimensional) throughout our experiments, the elastic vortex growth may

be the stable evolution of the flow with Wi rather than an elastic instability. That is, there is no evidence from the experiments of a Hopf bifurcation or a qualitatively different flow that would signal an instability as the Wi is varied. Nonetheless, for reference we calculate the value of the parameter M described by Eq. (1) corresponding to the value of Wi below which we do not detect vortices ($Wi_{\text{crit}}=0.84$; see Fig. 2). Estimating the elastic stress τ_{11} as $2\eta_p\lambda\dot{\gamma}^2$ based on the upper convected Maxwell fluid where η_p is the polymeric contribution to the solution viscosity at the critical shear rate and the radius of curvature for flow at the centerline of the microbend is determined from streak images to be $\sim 130 \mu\text{m}$, we find $M \sim 0.5$. That is, we observe vortex formation for $M > 0.5$. This numerical value of M is roughly an order of magnitude lower than the values of M_{crit} at which purely elastic instabilities have been observed in other geometries. On the other hand, this value of M indicates some modest coupling of streamline curvature and normal stresses, and so one cannot rule out the possibility of an elastic instability solely on the basis of this M value. A three-dimensional numerical simulation of this flow as a function of Wi , using the rheological parameters for the DNA solution used here, should resolve the question of the stability of this flow.

In summary, we find that for flows of a shear-thinning, viscoelastic DNA solution in a planar 90° microbend an elastic vortex forms at the inside upstream corner of the bend. This vortex grows with Wi and remains stable and steady over the Re and Wi range probed ($9.9 \times 10^{-7} < Re < 3.1 \times 10^{-2}$, $0.41 < Wi < 126$). Since microbends are canonical microfluidic elements that are commonly incorporated into lab-on-a-chip systems and μTAS , it is critical to characterize the viscoelastic behavior caused by the biological macromolecules used in these systems. Additionally, it is important for design and operation of these devices to understand the influence of elastic secondary flows that arise due to streamline curvature and abrupt changes in geometry on the shear rates and residence times experienced by macromolecules in these microdevices.

-
- [1] R. B. Bird, R. C. Armstrong, and O. Hassager, *Dynamics of Polymeric Liquids* (John Wiley & Sons, New York, 1987), Vol. 1.
- [2] R. G. Larson, E. S. G. Shaqfeh, and S. J. Muller, *J. Fluid Mech.* **218**, 573 (1990).
- [3] P. Pakdel and G. H. McKinley, *Phys. Rev. Lett.* **77**, 2459 (1996).
- [4] G. H. McKinley, P. Pakdel, and A. Oztekin, *J. Non-Newtonian Fluid Mech.* **67**, 19 (1996).
- [5] E. S. G. Shaqfeh, *Annu. Rev. Fluid Mech.* **28**, 129 (1996).
- [6] G. H. McKinley, W. P. Raiford, R. A. Brown, and R. C. Armstrong, *J. Fluid Mech.* **223**, 411 (1991).
- [7] L. E. Rodd, T. P. Scott, D. V. Boger, J. J. Cooper-White, and G. H. McKinley, *J. Non-Newtonian Fluid Mech.* **129**, 1 (2005).
- [8] L. E. Rodd, J. J. Cooper-White, D. V. Boger, and G. H. McKinley, *J. Non-Newtonian Fluid Mech.* **143**, 170 (2007).
- [9] S. Gulati, S. J. Muller, and D. Liepmann, *J. Non-Newtonian Fluid Mech.* **155**, 51 (2008).
- [10] J. A. Pathak, D. Ross, and K. B. Migler, *Phys. Fluids* **16**, 4028 (2004).
- [11] A. Groisman and V. Steinberg, *Nature (London)* **410**, 905 (2001).
- [12] T. Burghelca, E. Segre, I. Bar-Joseph, A. Groisman, and V. Steinberg, *Phys. Rev. E* **69**, 066305 (2004).
- [13] P. E. Arratia, C. C. Thomas, J. Diorio, and J. P. Gollub, *Phys. Rev. Lett.* **96**, 144502 (2006).
- [14] A. Groisman and V. Steinberg, *New J. Phys.* **6**, 2 (2004).
- [15] F. Schonfeld and S. Hardt, *AIChE J.* **50**, 771 (2004).
- [16] P. B. Howell, D. R. Mott, J. P. Golden, and F. S. Ligler, *Lab Chip* **4**, 663 (2004).
- [17] A. P. Sudarsan and V. M. Ugaz, *Lab Chip* **6**, 74 (2006).
- [18] A. P. Sudarsan and V. M. Ugaz, *Proc. Natl. Acad. Sci. U.S.A.*

- 103**, 7229 (2006).
- [19] M. G. N. Perera and K. Walters, *J. Non-Newtonian Fluid Mech.* **2**, 49 (1977).
- [20] S. Chono and Y. Iemoto, *J. Rheol.* **32**, 335 (1992).
- [21] T. Cochrane, K. Walters, and M. F. Webster, *J. Non-Newtonian Fluid Mech.* **10**, 95 (1982).
- [22] S. Chono and Y. Iemoto, *J. Rheol.* **34**, 295 (1990).
- [23] S. Gulati, Ph.D. thesis, University of California, Berkeley, 2006.
- [24] R. D. Blevins, *Applied Fluid Dynamics Handbook* (Van Nostrand Reinhold, New York, 1984).